Lateral ring compression test applied to a small caliber steel jacket: Identification of a constitutive model

Yann Coget, Yaël Demarty, Christophe Czarnota, Anthony Bracq, Jean-Sebastien Brest, Alexis Rusinek

Defence Technology xxx (xxxx) xxx

Contents lists available at ScienceDirect

Defence Technology

journal homepage: www.keaipublishing.com/en/journals/defence-technology

Lateral ring compression test applied to a small caliber steel jacket: Identification of a constitutive model

Yann Coget [a, b], Yaël Demarty [a, *], Christophe Czarnota [b], Anthony Bracq [a], Jean-Sebastien Brest [a], Alexis Rusinek [b]

[a] French-German Research Institute of Saint-Louis, 5 Rue Du Général Cassagnou, 68300 Saint-Louis, France
[b] Laboratoire d'Etude des Microstructures et de Mécanique des Matériaux (LEM3), CNRS, Université de Lorraine, Arts & Métiers ParisTech, F-57000 Metz, France

ARTICLE INFO

Article history:
Received 5 July 2023
Received in revised form
15 September 2023
Accepted 1 November 2023
Available online xxx

Keywords:
Full metal jacket ammunition
Lateral ring compression
Inverse identification
Numerical simulation

ABSTRACT

The evolution of threats and scenarios requires continuous performance improvements of ballistic protections for armed forces. From a modeling point of view, it is necessary to use sufficiently precise material behavior models to accurately describe the phenomena observed during the impact of a projectile on a protective equipment. In this context, the goal of this paper is to characterize the behavior of a small caliber steel jacket by combining experimental and numerical approaches. The experimental method is based on the lateral compression of ring specimens directly machined from the thin and small ammunition. Various speeds and temperatures are considered in a quasi-static regime in order to reveal the strain rate and temperature dependencies of the tested material. The Finite Element Updating Method (FEMU) is used. Experimental results are coupled with an inverse optimization method and a finite element numerical model in order to determine the parameters of a constitutive model representative of the jacket material. Predictions of the present model are verified against experimental results and a parametric study as well as a discussion on the identified material parameters are proposed. The results indicate that the strain hardening parameter can be neglected and the behavior of the thin steel jacket can be described by a modeling without strain hardening sensitivity.

1. Introduction

The constantly evolving ballistic threats enforce the improvement of ballistic protections, in terms of performance, weight reduction and wearing comfort. Ballistic tests are conventionally carried out to assess and validate the levels of protection. Conducting tests makes it possible to obtain information on the mechanisms occurring during the impact and characterize the macroscopic behavior of the protection (stopping of the ammunition, perforation, deflection of the rear face, etc.). Without any doubt, experimental tests are crucial and invaluable, but they remain time consuming (preparation of the different geometries, tests set-up, limited number of shots …) and limited in terms of the range of investigated impact conditions. As an alternate and complementary approach, a finite element-based method is useful to explore a larger range of situations, and develop a better understanding of fracture mechanisms during impact including the interaction with the behavior of the projectile at the local scale. The main advantage of numerical simulations lies in the possibility to evaluate a wide variety of configurations (loading amplitude, materials, geometry, architecture, etc.). In order to obtain reliable results, it is necessary to use sufficiently precise constitutive models to accurately describe the phenomena observed during the impact of a projectile on protective equipment. Our study focuses on a 9 mm small caliber ammunition with a ductile core, more specifically on the behavior of the steel alloy jacket. The goal is to identify a constitutive model using lateral compression tests on ring specimens taken from the steel jacket, keeping the material and microstructural properties originating from the forming process.

A jacketed bullet is a small caliber projectile made of a soft core (often lead as in the case of our study [1]) generally enclosed in a harder metal shell called an ammunition jacket [2]. It can be made

* Corresponding author.
E-mail address: yael.demarty@isl.eu (Y. Demarty).
Peer review under responsibility of China Ordnance Society

https://doi.org/10.1016/j.dt.2023.11.001

of different materials such as brass, cupronickel or less frequently a steel alloy [3–6]. Jacket is used to enhance the rigidity of the ammunition and to avoid deposition of metal into the barrel, so that higher speeds are reached at the exit. Usually, the mechanical characterization of a constitutive relationship for a steel alloy is performed using compression tests on cylindrical samples (milled from a raw plate or bar) at different strain rates and temperatures [3,5,7]. Various phenomenological, physical or semi-physical constitutive law parameters are then identified and subsequently used in numerical simulations. If this type of geometry allows materials characterization using well established experimental protocols, the identified constitutive law would probably not reflect the actual behavior of materials obtained from different processing routes.

In addition, when one needs to characterize materials including viscoplasticity, anisotropy, microstructural changes, a large number of tests are needed and the identification procedure based on direct approaches tends to be difficult. Coupling experimental measurements (from force-displacement curves or full-field measurements) with numerical simulations [8–10] or analytical approaches based on virtual field methods [11,12] has thus gained in popularity, see Ref. [13]. These inverse identification procedures are usually applied to complex geometries where heterogeneous fields develop and consequently a reduced number of tests are required to identify various sensitivities (e.g. strain rate, thermal) of a constitutive modeling. This coupling procedure can also be used to characterize the material's behavior of samples for which the geometry is dictated by the needs [14].

For the studied case, the jacket is formed through a thermo-mechanical process which consists of successive metal punching and drawing operations. In order to preserve the microstructure and the thermo-mechanical history inherited from the manufacturing process, ring specimens corresponding to the steel jacket were extracted from the ammunition. The cylindrical geometry, with various shapes of the cross sections, has been largely considered in the context of crashworthiness studies to optimize the energy absorption capabilities of components used in transportation systems and subjected to axial static [15] or dynamic loading [8,16].

Lateral compressive experiments on rings and tubes have also been considered in the literature [17–19], particularly for nuclear material research where it is used as a screening test to determine material ductility in the circumferential direction [20]. Within a different context, Ref. [21] combined a Finite Element model with an inverse identification approach to identify a power-law strain hardening law describing a brass alloy. As a numerical output, the authors used load/deflection curves in the inverse identification loop, combined to an analytical approach which relates the strain hardening parameters and the plastic modulus.

In Ref. [22], lateral compression tests were carried out to analyze the influence of heterogeneities introduced into the constitutive model of an aluminum alloy. An inverse method was also used for the determination of material constitutive law parameters. In their work, the authors considered two strain hardened material models: a power law [21,23] and a hybrid model assuming a linear saturated strain hardening but including a statistical description of the yield stress. In line with the scope of the present work, following the work of [14,21] used lateral compression tests and inverse identification method for the characterization of a 12.7 mm AP ammunition composed of a brass jacket and high-strength steel core. The authors showed that the method is relevant and gives accurate results for the 12.7 diameter ammunition.

It is reported in the literature that there are analytical methods which allow to obtain the Young modulus, the yield stress and the stress-strain behavior from lateral compressive experiments on rings [24,25]. However, these analytical approaches are valid for some specific geometrical conditions where the thickness to diameter ratio verifies $0.1 \leq t/d \leq 0.4$.

Characterizing the behavior of thin rings (thickness to diameter ratio <0.05) made of steel, directly extracted from the jacket of ammunition is a field of research which is not fully explored and requires more attention. If the protocol used here is well inspired from a previous work of our research group [14], the characterization of material properties from a very thin walled ring is very challenging. To this end, the purpose of the present work is to identify a constitutive model of the 9 mm steel jacket (directly extracted from the ammunition) from an inverse approach coupled with finite element calculations. The specimens will be subjected to low loading rates and moderate temperatures. Even if the material is characterized in these regimes, the constitutive relation and identification provide a set of material parameters which describe materials and components used in ballistic impact. Indeed, the set of identified parameters has been successfully employed to describe, with sufficient accuracy, the dynamic response of a projectile composed of lead core and this steel jacket. This validation underscores the practical utility of the findings of the present paper. In addition, experimental results and analysis reported in this paper may help designers of protective equipment against 9 mm steel jacket ammunition.

The present manuscript is organized as follows. In Section II, the material chemical composition is first presented followed by hardness results revealing the homogeneity of the tested material. The section ends with the detailed experimental program carried out in this work. Section III begins with the inverse approach implemented for the model parameter identification. Then, the finite element model using Abaqus/Standard is described. All results (experimental followed by identified parameters and a comparative analysis) are next provided in Section IV. Material sensitivities to strain rate and temperature are analyzed and quantified. In order to evaluate relevancy of identified values of the parameters, a parametric study is finally proposed in Section V where the influence of strain hardening parameters are examined.

2. Description of the bullet jacket and lateral compression protocol

2.1. Description of the bullet jacket: materials and geometry

The jacket corresponding to the outer shell of the 9 mm bullet, studied in this paper has a density of 8050 kg/m^3. It is made of a mild steel alloy plated on both faces with tombac which is a brass alloy used to improve the sliding properties between the munition and the barrel of the weapon. Fig. 1(a) shows a cross section of the bullet composed of a soft inner core made of lead and the outer jacket. Measurements made on the munition with a Field Emission Scanning Electron Microscope (FE-SEM Thermofisher NNS450) revealed an external diameter of 9.00 ± 0.01 mm and a thickness of 0.35 ± 0.01 mm for the jacket (steel and tombac), see Fig. 1(b). The thickness of each tombac layer is approximately 0.025 mm, which infers that the thickness of both layers represents about 14% of the jacket thickness. Considering the low proportion of tombac, this coating layer is assumed to have a limited influence on the overall mechanical response and a single material model will be identified to describe the whole response of the jacket.

2.2. Hardness testing and analysis of homogeneity

Vickers microhardness indentations were conducted with a load of 1 kgf on a polished cross-section using a micro-hardness tester Wilson® VH 1202 Buehler. The diamond indenter has an angle of

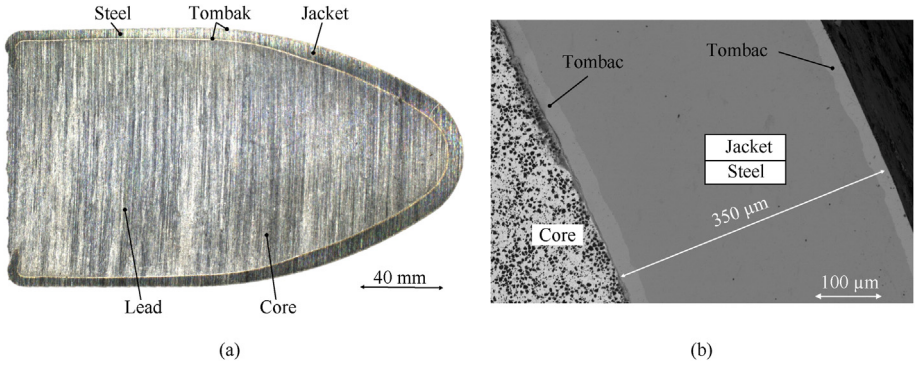

Fig. 1. (a) Cross-section of the 9 mm ammunition made of lead-core and a steel casing plated with tombac; (b) SEM observation of the jacket (steel in dark grey and tombac in light grey).

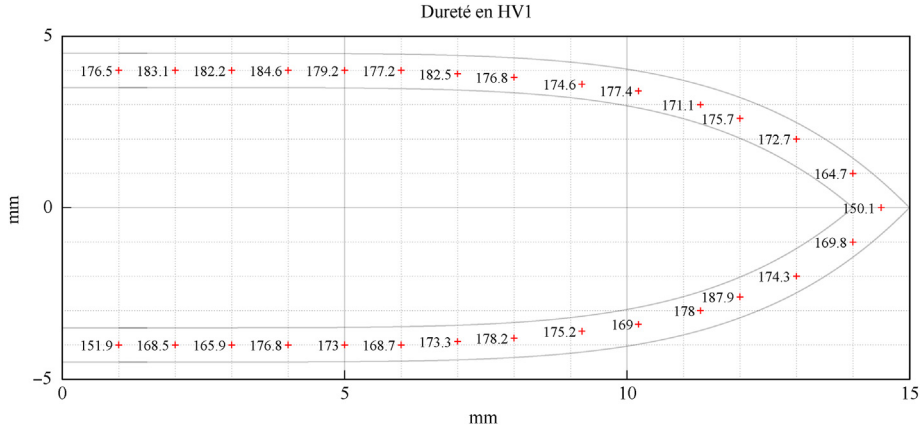

Fig. 2. Microhardness map (unit HV1) of the jacket cross section. Measurement points (red symbols) are located within the steel.

136° between opposite faces. Fig. 2 shows the indentation locations all along the cross-section. Twenty-nine measurements were done at regularly spaced positions along a path at a mid-distance of the jacket borders. Based on it, the average value may be considered as representative of the mechanical property. A unique specimen was used for microhardness testing, for which, as shown in Fig. 2, a rather homogeneous hardness is observed. A mean value of 173 HV1 and a standard deviation to the mean of 22 HV1 have been defined.

The measured values can give a rough estimate of the elastic limit σ_y of the jacket steel from linear equations involving the diamond pyramid hardness H_v [26,27]. For instance, using the following relationship [26], the yield stress may be estimated.

$$\sigma_y = -90.7 + 2.876H_v \quad (1)$$

In this work, using a specific bullet, the value is $\sigma_y = 406.8 \pm 64.3$ MPa. Note that Eq. (1) has been verified for over 150 steels having a wide range of compositions and a variety of microstructures and that the other properties have been defined using mechanical tests [26].

2.3. Ring lateral compression tests description

2.3.1. Specimen geometry design and preparation

The exact composition of the jacket materials as well as the manufacturing process and thermal treatment are unknown. The determination of an accurate constitutive relation aiming to describe the jacket behavior in a ballistic impact implies to extract samples from a material which has undergone identical thermo mechanical processes. Following the approach of [14], the samples were machined directly from the original ammunition. The final geometry of specimens corresponds to a thin-walled tube of height 6.00 mm (±0.03 mm), diameter 9.00 mm (±0.01 mm) and thickness 0.35 mm (±0.01 mm) (see Fig. 3). This geometry has been adopted to examine the response of ring specimens under lateral compression considering five different loading conditions in terms of temperature and traverse speeds. This is detailed in the next section.

2.3.2. Experimental set-up and testing conditions

The first step of the characterization process is to acquire the experimental data set necessary to identify the parameters of the constitutive relation. All ring lateral compression tests were carried out under quasi-static regime on an Instron® 5982 universal press equipped with a 1 kN load cell. The load cell allows to measure the force imposed to the ring while the traverse displacement sensor provides from the global displacement. Compression tests were performed up to a crosshead displacement of 5 mm. Dependencies with the strain rate in quasi-static regime and temperature were analyzed by considering different conditions in terms of traverse speed and sample temperature, see Table 1. We conducted a total of two tests for each of the five loading conditions. While our initial intention was to perform three replicate tests per condition to account for test error and data scatter, the amount of material limited us to two tests. Additionally, it is important to note that the replication of test results was in the maximum range of 10%.

We believe that the identified parameters, as reported in this

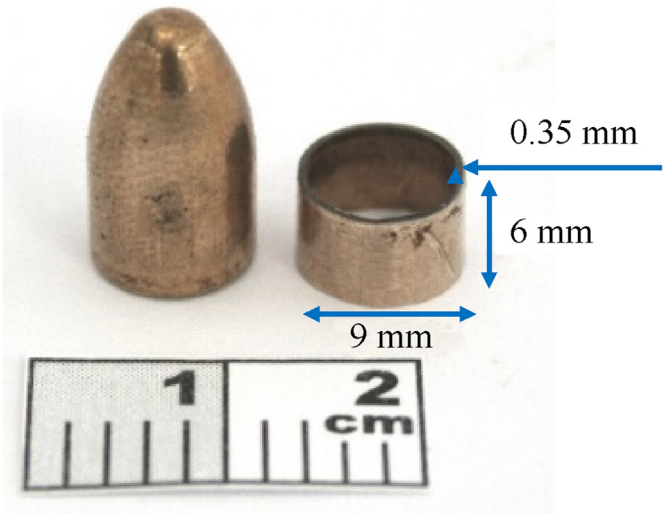

Fig. 3. 9 mm ammunition and specimen after preparation (machining and soft core removal).

Table 1
Experimental conditions of the ring lateral compression experiments.

Experiment #	1	2	3	4	5
Traverse speed/(mm·min^{-1})	1	3	10	3	3
Temperature/K	293	293	293	373	473

study, will only require slight adjustments when based on a larger dataset. The analysis and methodology remain consistent with the work of [14], where the same methodology has proven its effectiveness.

Tests at elevated temperatures were conducted by heating the samples using a Steinel 2300 W heat gun while the temperature of tested samples was controlled by a thermocouple positioned on the inner face. It should be noted that the homogeneity of the temperature field has been verified, in advance, using multiple thermocouples glued on one sample. A camera Basler acA 1920-40 g with a 1220 1920 × 1200 pixels resolution and a recording frame rate set to 10 fps as well as a lighting device were used to record the shape geometry evolution during experiments.

3. Inverse identification of constitutive model parameters using an optimization algorithm

3.1. Description of the constitutive relation used for numerical simulations

Metals and more specifically steel alloys used for armor protection or bullet cores are well-known materials and were very often studied in the literature under static and dynamic regimes [7,28–30]. However, there is a constant need to precisely identify constitutive relations for steel alloys specifically dedicated to ammunition components. The knowledge of the constitutive relation is the key point for numerical simulations. It has to be noticed, that numerous constitutive models, based on physical or phenomenological approach, have been developed to describe the dynamic behavior of materials such as Refs. [31–33]. For the 9 mm ammunition jacket, the phenomenological Johnson-Cook model is adopted in the present work. This model, which is already implemented in most finite element codes, is widely used for the simulation of ballistic impacts where strain rate sensitivities and temperature dependencies are observed [34]. In this model, the equivalent plastic stress σ is expressed as

$$\sigma = (A + B\varepsilon^n)\left[1 + C\ln\left(\frac{\dot{\varepsilon}}{\dot{\varepsilon}_0}\right)\right]\left[1 - \left(\frac{T - T_0}{T_m - T_0}\right)^m\right] \quad (2)$$

where ε is the equivalent plastic strain, $\dot{\varepsilon}$ is the plastic strain rate and T the temperature. $\dot{\varepsilon}_0$ is a reference strain rate, T_0 a reference temperature and T_m being the material melting temperature. The parameter A is the initial yield strength of the material at the reference strain rate and for a reference temperature. B and n represent the strain hardening while C and m describe the strain rate and thermal sensitivities respectively.

3.2. Identification of constitutive model parameters: inverse method coupled with finite element simulation and an optimization procedure

It is important to know that the determination of conventional stress-strain curves is not trivial since a lateral compression test on rings is used. Therefore, a straightforward identification of material parameters involved in Eq. (2) is not possible. An attempt was proposed in Ref. [25] where the authors developed a model using compressed metal rings with isotropic properties coupling to a power law. The approach proposed was validated for thickness to diameter ratios varying as $0.1 \leq \frac{t}{\varnothing} \leq 0.4$. In our study, as the ratio is lower than 0.04 and falls out the range of validity of the theoretical approach of Ref. [25], the process of identification to define the model parameters was based on an inverse method. More precisely, a Finite Element Updating Method has been considered [35], coupling the FE solver Abaqus/Standard and the standalone optimization package from LS-OPT. The formulation of LS-OPT (in charge of the automatic identification) relies on the minimization of a multi-objective function $F(\Phi_1, \Phi_2, \ldots, \Phi_N)$ expressed as

$$F = \sum_{k=1}^{N} \Phi_k \quad (3)$$

where N is the number of objectives and $\Phi_k = \Phi_k(\boldsymbol{x})$, $k = 1 \ldots N$, represents the kth objective function, $\boldsymbol{x}$ being the vector parameters. Based on the Mean Squared Error's (MSE) method, $\Phi_k(\boldsymbol{x})$ is written as

$$\Phi_k = \frac{1}{P_k}\sum_{j=1}^{P_k}\left[\frac{C_{k,j}(\boldsymbol{x}) - T_{k,j}}{\max\left|T_{k,j}\right|}\right]^2 \quad (4)$$

where P_k stands for the number of points on the target experimental curve T, with $T_{k,j}$ the corresponding values and $C_{k,j}(\boldsymbol{x})$ the respective components of the computed curve $\mathscr{C}$. The technique implemented in LS-OPT and used to minimize F in Eq. (3) is based on the Kriging metamodeling technique [36]. In addition, the accuracy of the metamodel was improved by a successive response surface method (SRSM) in which the size of the subregions over which the objective function is evaluated is reduced until convergence. More details can be found in Ref. [37].

The measurements used in the optimization procedure are directly taken from the compression experimental data *i.e.* the cell force and the traverse displacement. From the experimental measurements, the iterative approach consists of approximating the model's parameters to get the best match between numerical results and experimental data [38,39]. After each iteration, LS-OPT© compares the numerical results with the experimental ones and adjusts the parameter values for the next iteration until the

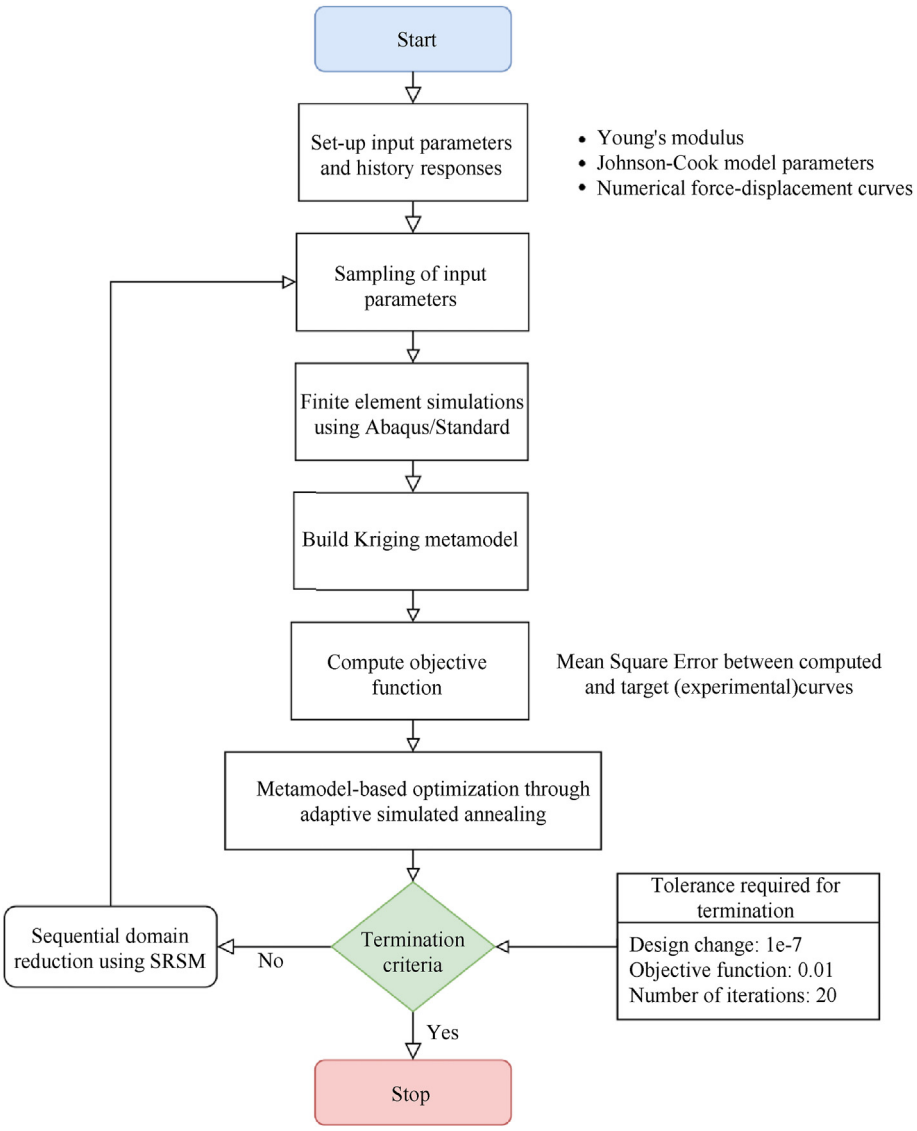

Fig. 4. Diagram depicting the optimization method using the inverse method for Johnson-Cook model parameters identification.

termination criteria are reached. In addition, for a rheological identification problem, an appropriate domain of parameter values having a physical sense must be introduced so that the optimization problem is formulated as, see Ref. [39].

$$\begin{cases} \min\limits_{\boldsymbol{x}\in D(\boldsymbol{x})} F(\boldsymbol{x},\boldsymbol{C},\boldsymbol{T}) \\ D(\boldsymbol{x}) = \{\boldsymbol{x} | \boldsymbol{x}_{\min} < \boldsymbol{x} < \boldsymbol{x}_{\max}\} \end{cases} \tag{5}$$

The upper and lower limits are thus very important to prevent the parameters to reach non-physical values. To obtain more precise values, it is possible to compute several optimization loops refining the bounds of each parameter.

The diagram reported in Fig. 4 details the method used for the determination of the Johnson-Cook constitutive model parameters of the steel jacket.

For this optimization routine, some material model parameters have been kept constant as the Poisson's ratio (set to 0.3), the melting temperature T_m, reference temperature T_0, reference strain rate $\dot{\varepsilon_0}$. The values are the following: $T_m = 1793$ K, $T_0 = 293$ K and $\dot{\varepsilon_0} = 0.0003$ s-1, Eq. (2). Finally, six parameters of the material law are unknown in the numerical model. Indeed, five parameters of the constitutive relation (A, B, n, C, m) and one of the elastic properties, the Young's modulus (E) need to be identified through the optimization process. It is reminded that the density of the material has been measured to 8050 kg/m3 and the Poisson's ratio has been set to 0.3. The five experimental conditions listed in Table 1 are simulated using Abaqus/Standard considering the Johnson-Cook model to describe the jacket material response.

Three objective functions, i.e. $N = 3$ in Eq. (3), are introduced to consider the strain hardening, the strain rate sensitivity and the thermal softening observed in Fig. 10.

- Φ_1 stemming from the force-displacement curve obtained at 3 mm/min and 293 K for the identification of the hardening parameters of the Johnson-Cook model (A, B and n in Eq. (2) and the Young's modulus).
- Φ_2 built from data points collected at a constant displacement of 3 mm on force-displacement curves obtained at various speeds and room temperature. These data, lying on the plateau part are used to identify the strain rate dependence (parameter C in Eq. (2)).

- Φ_3 defined from measurements taken at a constant displacement of 3 mm on force-displacement curves obtained at a constant traverse speed of 1 mm/min under various temperatures. As for Φ_2, these points are located on the plateau part and they are used here to identify the thermal sensitivity of the material (parameter m in Eq. (2)).

Eight optimization loops, each involving fifty iteration steps, were necessary to reach the convergence of model parameters. The value of the multi-objective function at the end of the optimization procedure were the number of iteration (set to 20) and/or the objective function lower than a value (<0.01) (see Fig. 9).

3.3. Description of the finite element model of the lateral compression test

Three-dimensional finite element calculations were conducted using Abaqus/Standard. One eighth of the ring specimen presented in Fig. 5 is meshed using 1200 linear hexahedral elements with reduced integration (C3D8R from the in-built element library of Abaqus/Standard). A mesh-size sensitivity study has been conducted (results not shown here) which exhibited that the minimum required number of elements in the thickness is four. This number is sufficient to describe buckling and bending of the structure [40]. The tools are modelled by analytical rigid surfaces. The interaction between contacting surfaces is defined using the isotropic Coulomb friction model with a standard friction coefficient set to 0.2. This adopted value is discussed in section V.1. The boundary conditions used are presented on Fig. 5. They consist of symmetries about 1-, 2- and 3-directions and imposed velocity on the upper rigid surface. The material is thermo-elastic-viscoplastic (linear elasticity) following von-Mises plasticity with isotropic hardening, the yield stress being given by Eq. (2). Due to large deformation, geometrical nonlinearities are accounted in the numerical modeling. Depending on the loading configuration (see Table 1), an initial temperature is applied to the material nodes. The displacements being imposed at the upper tool, corresponding reaction forces are computed in order to build the multi-objective function F, see Eqs. (3) and (4).

The macroscopic simulation allows to obtain local values and to understand in a better way the kinematic of the structural test.

4. Experimental results and identification of constitutive model parameters

4.1. Force-displacement curves and ring deformation

4.1.1. Analysis of the force-displacement curves

The test performed with a constant velocity of 3 mm/min and $T = 293$ K is first analyzed. Fig. 6, displaying the force versus time graph shows that the deformation curve can be schematically divided into four stages. Stage I corresponds to a linear increase of the force (from $t = 0$–8 s) and is governed by the elastic response of the material. Stage II shows a gradual increase of the force which is reflecting the inception and early accumulation of plastic deformation within the sample (8–22 s). Stage III (from 22 s to about 75 s) is defined by a linear growth of the force and during the last Stage IV, the force is non-linearly increasing with time up to the complete crushing of the specimen and corresponding to compaction.

On the following curves, the loading speed effect and temperature are illustrated Figs. 7(a) and 7(b) respectively. As a peculiar observation, it is worth noting from Fig. 7(a) that the elastic parts obtained at loading rates of 3 mm/min and 10 mm/min closely coincide with each other. However, the structural elastic response obtained at a loading rate of 1 mm/min appears to exhibit a slightly

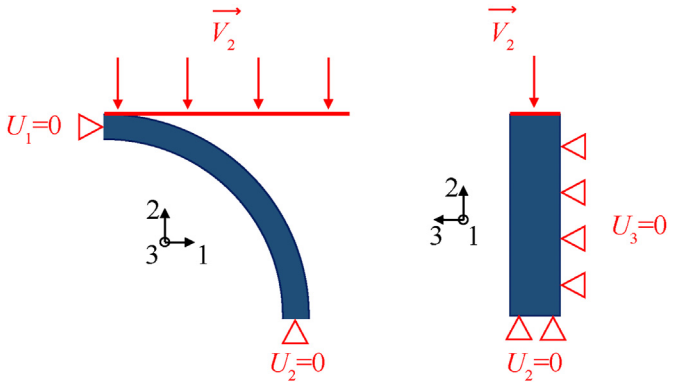

Fig. 5. Representation of one eighth of the sample and applied boundary conditions for lateral compression of ring.

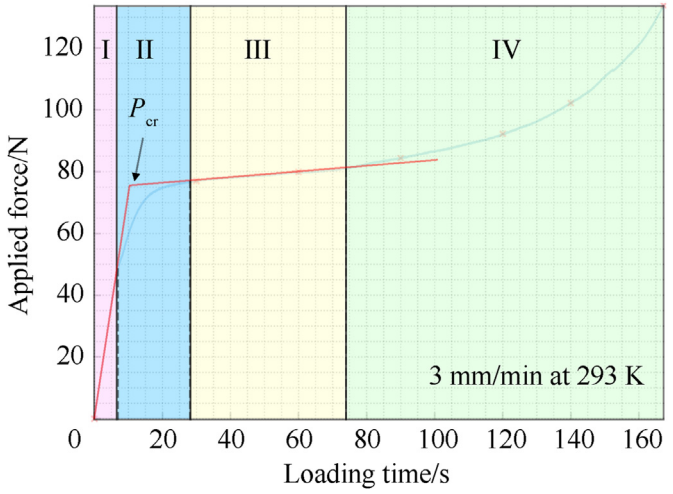

Fig. 6. Force versus time for a compression test conducted at a traverse speed of 3 mm/min and room temperature (293 K). The force in the compression test does not start from zero due to initial contact forces. The plot begins at the point where significant deformation begins. Red cross mark times of recorded snapshots reported in Fig. 8.

softer behavior. This variation in the elastic region may be attributed to a combination of factors, including variations in material properties, specimen preparation, specimen geometry, contact initiation.

Any variations in the elastic region are believed to not significantly impact our analysis and the material parameters of the Johnson Cook law identified in our study. The comparison of the different tests conducted for a constant temperature 293 K and varying the traverse speed reveals the material's strain rate sensitivity in the low strain rate regime. It is shown on Fig. 7(a) that higher the speed induces a force increase. Similarly, the tests conducted at 3 mm/min for different initial temperatures induce a thermal softening effect.

In addition to the mechanical tests the kinematic of the ring has been analyzed.

4.1.2. Kinematics of the deformation of the ring

The shape of the specimen and the characteristics contact are continuously linked during the deformation process. It can be observed in Fig. 8 for a test conducted at 3 mm/min and room temperature. During the test, the initially annular sample ($t = 0$ s) evolves, takes an oblong shape and further transforms into a bow tie. In addition, the contact zones (between the sample and the

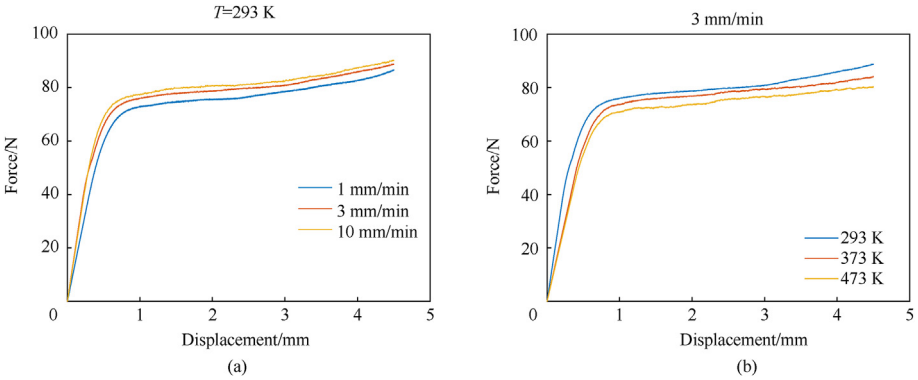

Fig. 7. Force-displacement curves: (a) at constant temperature (293 K) for 3 displacement speeds; (b) at constant displacement speed (3 mm/min) for 3 temperatures.

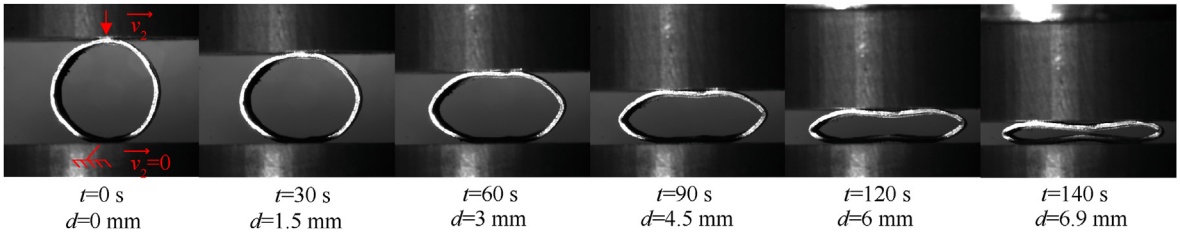

Fig. 8. Evolution of the cross-section for the test conducted at 3 mm/min and 293 K.

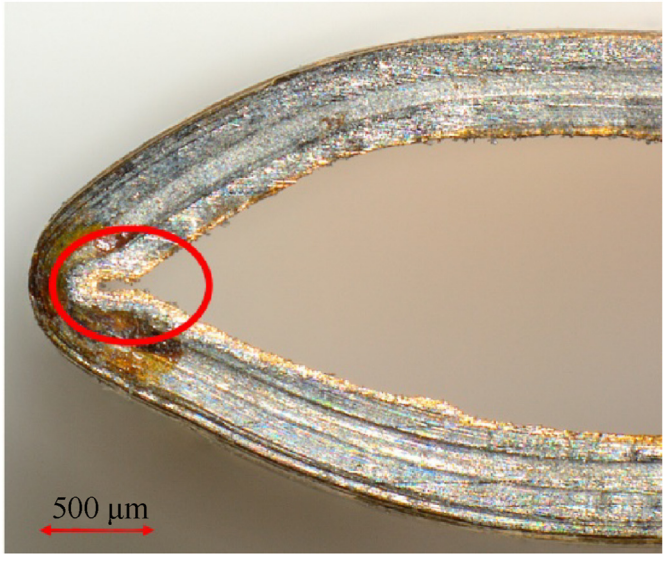

Fig. 9. Observation of a folding instability occurring in a specimen submitted to lateral compression at 3 mm/min and $T = 293$ K.

platens) move from the center to the periphery due to the neck shape observed in the middle of the ring. As a result, the moment-arm length is reduced which causes the load to increase as platen displacement increases [20].

For the displacements greater than 4 mm, larger deformations are achieved and structural instability emerges, as illustrated in Fig. 9. This instability, leads to the occurrence of folds in the sample at the place where lateral plastic hinges develop. The time at which the instability develops and the peculiar shape of the folds may depend on the loading condition, the geometry of the sample and materials (e.g. the mismatch between the steel core and tombac layer mechanical properties). It is important to note that the identification procedure we employed primarily centered on the material's response prior the onset of folding occurred.

Using all the tests described before and coupling different data, the constants of the Johnson Cook model and the Young's modulus may be defined from the finite element updating method.

4.2. Identification of material parameters from the inverse procedure

Experimental results presented in the previous section in terms of force versus displacement curves are used for the optimization routine. The three target experimental curves, $\mathscr{C}_{1,T}$, $\mathscr{C}_{2,T}$ and $\mathscr{C}_{3,T}$ related to Φ_1, Φ_2 and Φ_3 respectively, and defined in Eqs. (3) and (4), are reported in Fig. 10. Note that Φ_2 and Φ_3 are based on experimental points within Stage III, prior the instability takes place in the ring.

Initial values and bounds of each parameter have been taken from the literature [3,41,42], to obtain realistic parameters for a steel alloy. The values are given in Table 2.

Fig. 11 shows the evolution of the various parameters (red color curves) during the final loop of optimization. The bounds of the research domain, which are shown to evolve with the iteration step, are represented with blue and yellow solid lines. Note that, as a result from previous loops of optimization, these bounds at the initial iteration step may strongly differ from values reported in Table 2. The results of Fig. 11 shows that the parameters tend towards bounded values which guarantees accurate convergence and reliable results.

The values of Johnson-Cook model parameters obtained in the present study with $T_0 = 293$ K, $T_m = 1793$ K, $\dot{\varepsilon}_0 = 0.0003$ s^{-1}, and those reported in the literature, are summarized in Table 3.

Except for the set (B, n) characterizing the material strain hardening, other parameter values identified in our study are in good agreement with those found in the literature for mild steels [3,7]. The influence of deformation history on material parameters

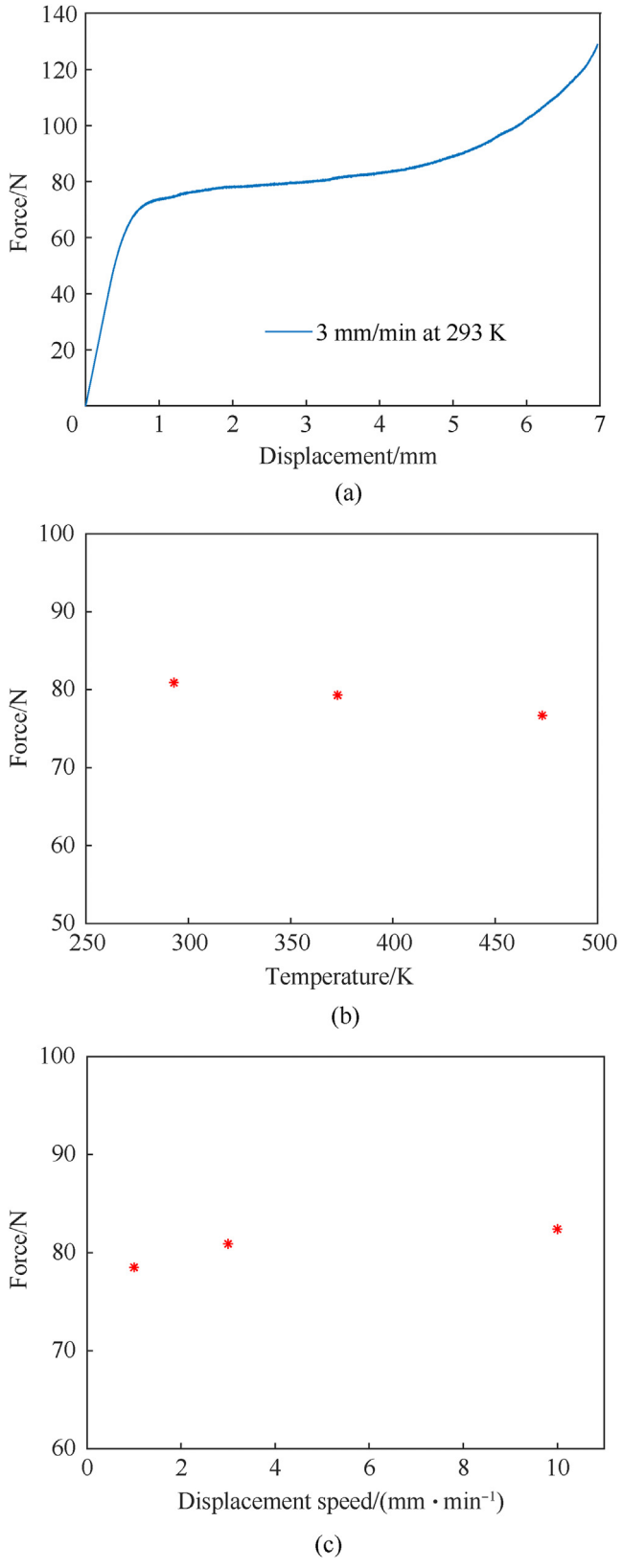

Fig. 10. Target experimental curves: (a) $\mathscr{C}_{1,T}$ corresponding to the force-displacement curve obtained at 3 mm/min and 293 K; (b) $\mathscr{C}_{2,T}$ corresponding to the force measured at a displacement of 3 mm on experiments #1, #2, #3; (c) $\mathscr{C}_{3,T}$ corresponding to the force measured at a displacement of 3 mm on experiments #1, #4, #5.

Table 2
Initial values and bounds for the optimization process.

	A/MPa	B/MPa	n	C	m	E/GPa
Initial values	350	275	0.36	0.0022	1	190
Initial bounds	[0–500]	[0–400]	[0–1]	[0.00–0.05]	[0–1.5]	[160–220]

could explain the large discrepancy observed for the hardening parameters. In fact, the material studied here has undergone hardening and possible thermal treatment while the jacket was formed. Another explanation may be found in the diametral compression test. A discussion is proposed in section V.2. The temperature sensitivity parameter ($m = 1.25$) is also a little bit more pronounced. The value of $A = 389$ MPa, which stands as the elastic yield limit (at $T = T_0$, $\dot{\varepsilon} = \dot{\varepsilon}_0$), is lower the average value, $\sigma_y = 406.8 \pm 64.3$ MPa, estimated using hardness measurements and Eq. (1). The value of A is consistent with the analytical approach proposed by Ref. [43] for a tube subjected to a radial compression. In this work of Ref. [43], the yield stress is expressed as

$$\sigma_y = \frac{\alpha_{cr} P_{cr} r_0}{e_0^2 l_0} \tag{6}$$

where α_{cr} is a parameter equal to 0.886, r_0 the initial inner radius of the tube, l_0 its length and e_0 its thickness. P_{cr} is the collapse load, corresponding to the intersection of the tangent of the plastic zone to the tangent of the elastic zone on the experimental force-displacement curve. Considering the specimen geometry $r_0 = 4.5$ mm, $l_0 = 6.3$ mm, $e_0 = 0.35$ mm and the collapse load $P_{cr} = 75$ N, estimated from Fig. 6, one obtains $\sigma_y = 388.7$ MPa. This value is very close to the value of A obtained from the optimization procedure.

Finally, based on the value of the strain hardening sensitivity n and the low value of B, the constitutive relation to define the jacket submitted to diametral compression may be reduced to

$$\sigma = A\left[1 + C\ln\left(\frac{\dot{\varepsilon}}{\dot{\varepsilon}_0}\right)\right]\left[1 - \left(\frac{T - T_0}{T_m - T_0}\right)^m\right] \tag{7}$$

with A, C, m listed in Table 3.

In order to validate the identification procedure and constitutive model parameters obtained in the previous part, numerical simulations of compression tests were conducted using the identified parameters of the Johnson-Cook model (see Table 3). Recall that the force-displacement curve obtained at 3 mm/min and 293 K and only one result point per other configurations were used in the identification procedure. Consequently, a comparative analysis of numerical and experimental force-displacement curves is first proposed in this section for loading configurations of Table 1. The evolution of the cross-section is also compared for one case. Numerical simulations are next used to examine stresses and strains within the specimen along with the evolution of the cross-section. We wish to clarify that the numerical modeling employed in our study was not able to capture the specific folding behavior shown in Fig. 6. Our primary focus in the numerical simulations was to investigate the deformation behavior prior the folding emerged.

The comparisons between experimental and numerical results are shown in Fig. 12 in terms of force versus displacement curves obtained for all tested configurations. One can observe that there is a good correlation between numerical curves and experimental results. The gradual increase of the force during Stage II (see Fig. 6) and its linear increase observed in Stage III are well described whatever the speed or temperature. Nevertheless, some differences are noticeable, mainly in the elastic zone (Stage I) due to sample

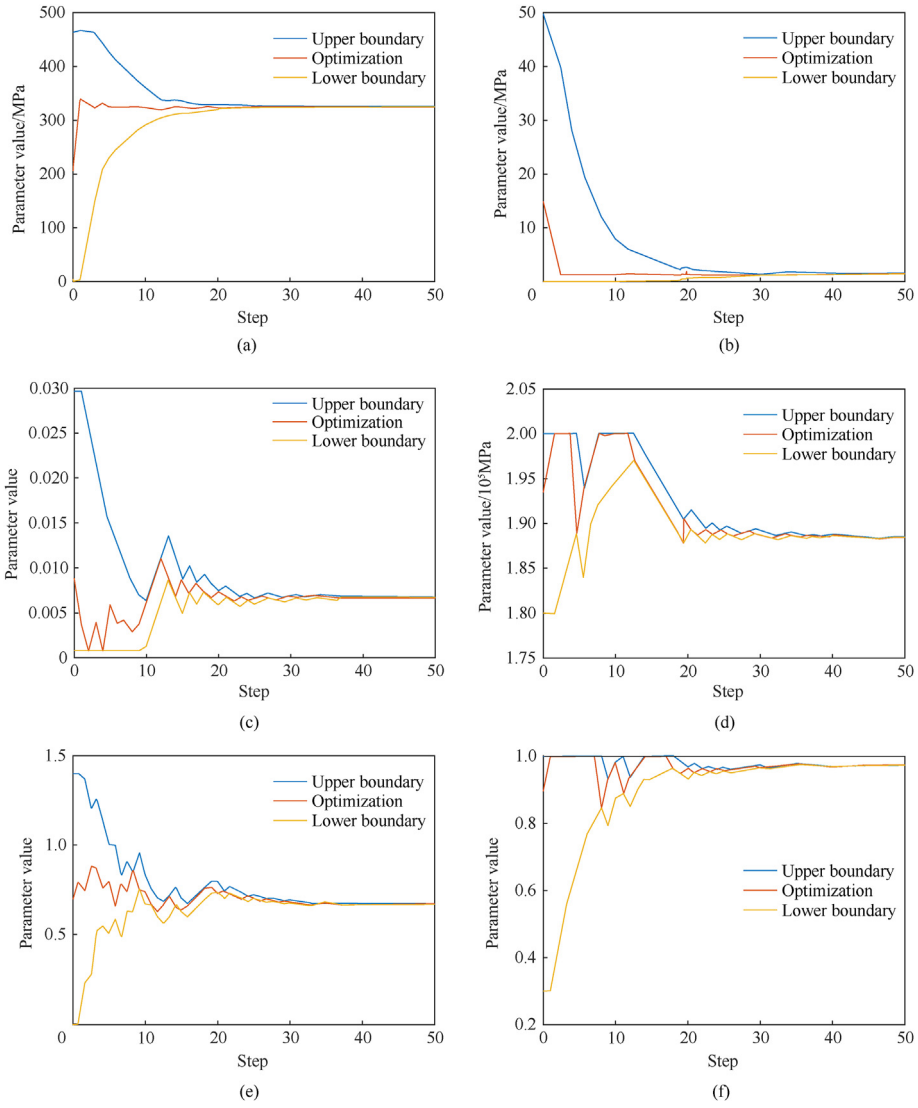

Fig. 11. Evolution of Johnson-Cook parameters and Young modulus during the last loop of optimization: (a) Convergence for the parameter *A*; (b) Convergence for the parameter *B*; (c) Convergence for the parameter *C*; (d) Convergence for the parameter *E*; (e) Convergence for the parameter *m*; (f) Convergence for the parameter *n*.

Table 3
Comparison of identified parameters and published data.

	E/GPa	*A*/MPa	*B*/MPa	*n*	*C*	*m*
Present study	189	389	1	0.96	0.013	1.25
S355NL steel [7]	190	353	590	0.32	0.024	0.85
1006 steel [3]	206	350	275	0.6	0.022	1.00

geometry variability and when high displacements are concerned (Stage IV).

A comparative analysis is also proposed in Fig. 13 showing, for the test at a displacement speed of 1 mm/min and room temperature (293 K), a proper consistency between the snapshots taken with the camera and the front cross section obtained from numerical simulations. This result also provides validation of the FE analyses along with the identified parameters.

The next step is to examine the local stress and strain distribution obtained for a traverse speed of 3 mm/min, at room temperature (293 K). First, it is important to mention that numerical simulations naturally account for the complex loading state which develops during deformation. As a consequence, the numerical force-displacement curve presented in the manuscript reflects the influence of shear and bending stresses within the specimen, which develop at boundaries where contact occurs and along its curved section, respectively. The extent to which shear and bending stresses develop can depend on various factors, including the material properties, geometry of the ring, loading conditions, and boundary constraints. Let us now focus on Fig. 14 which presents the equivalent plastic strain field (PEEQ) and the von Mises stress fields (σ_{vm}) inside the ring for $t = 4$ s, 33 s and 130 s.

This result gives an indication on the localization of plasticity areas. One observes that plasticity is initiated and first develops at the tool contact zones in the region aligned with the loading direction ($t \approx 4$ s/$d \approx 0.2$ mm) where the equivalent stress reaches a value of ≈ 395 MPa ($\sigma_{vm} > A \approx \sigma_y$). As observed in experiment (see Figs. 8 and 13), the contact with the upper tool quickly splits with contact areas moving away from each other (the same applies for the lower tool). Plastic deformation next localizes ($t \approx 33$ s/$d \approx 1.65$ mm) at lateral regions of the specimen where it further develops prior to a marked changed of the cross section of the cylinder which turns into a bow tie shape. At the end of the test ($t = 130$ s/$d = 6.5$ mm) the accumulated plastic strain and the von

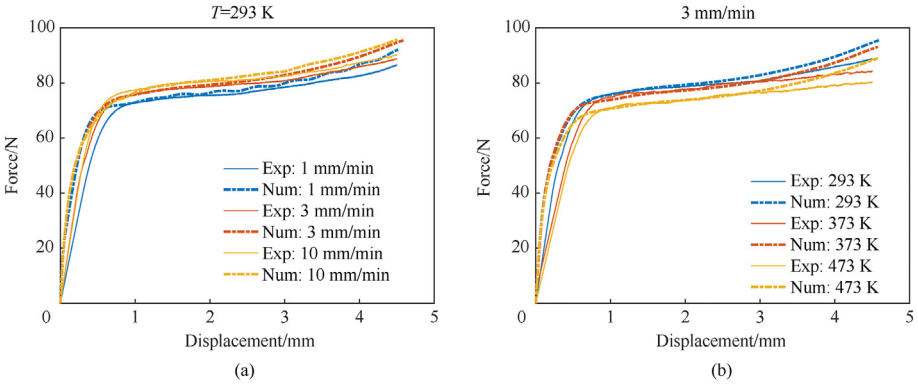

Fig. 12. Comparison of force-displacement plots between the experimental and numerical results at: (a) Constant temperature (293 K); (b) Constant displacement speed 3 mm/min.

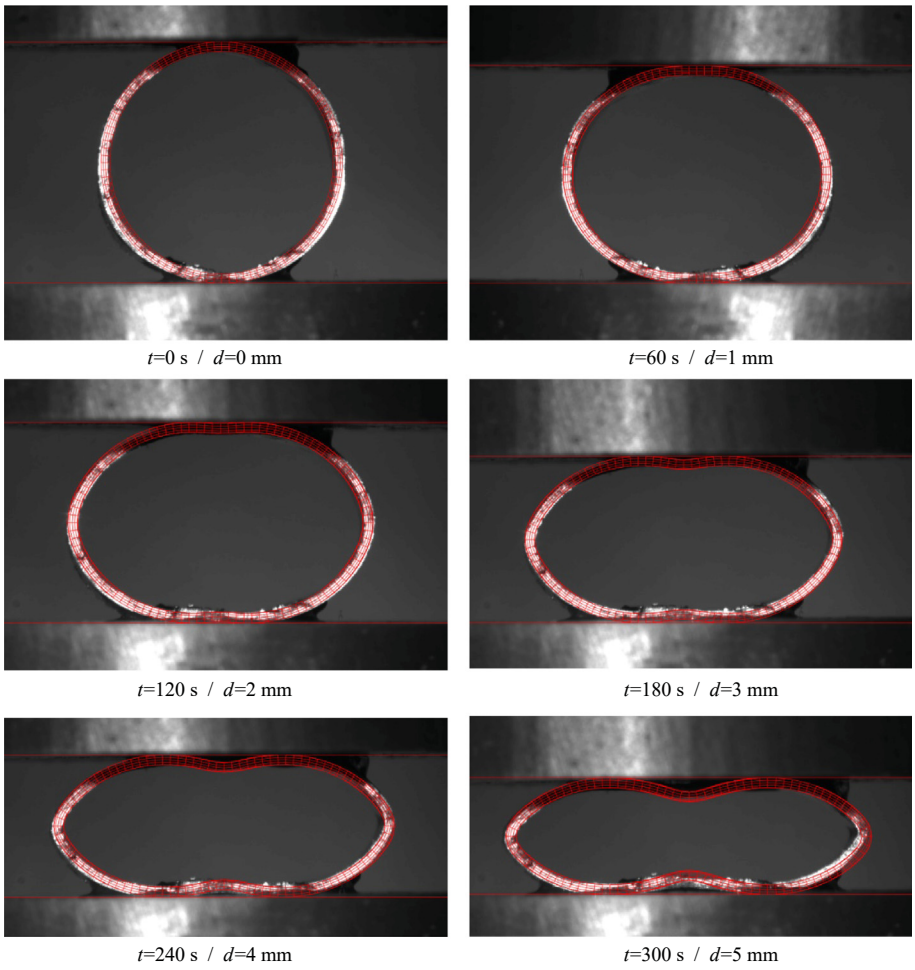

Fig. 13. Comparison of numerical cross-sections overlayed with experimental images for the test at a traverse speed of 1 mm/min and sample temperature of 293 K.

Mises stress increase to reach a maximal value of 0.29 and 401 MPa respectively, on the lateral regions of the specimen. It thus appears that in regions where plastic flow occurs, the equivalent stress is a bit larger than the initial yield stress $A = 389$ MPa. Since strain hardening effect is negligible (low value of B in the constitutive law), this can be attributed to the strain rate sensitivity of the material.

Despite some differences between numerical and experimental results, the comparative analysis is satisfactory. In fact, the simulation is an ideal case scenario which considers perfectly cylindrical specimens. By contrast, geometrical imperfections can be observed in specimens used in experiment as reflected at $t = 0$ s on Fig. 13. This may be at the origin of some discrepancies between experimental and numerical results. However, it is noteworthy that the set of identified parameters demonstrated its effectiveness in reproducing the dynamic response of ammunition, as detailed in Ref. [2]. In this study, Split Hopkinson Pressure Bar (SHPB) tests were conducted on the lead core and steel jacket assembly,

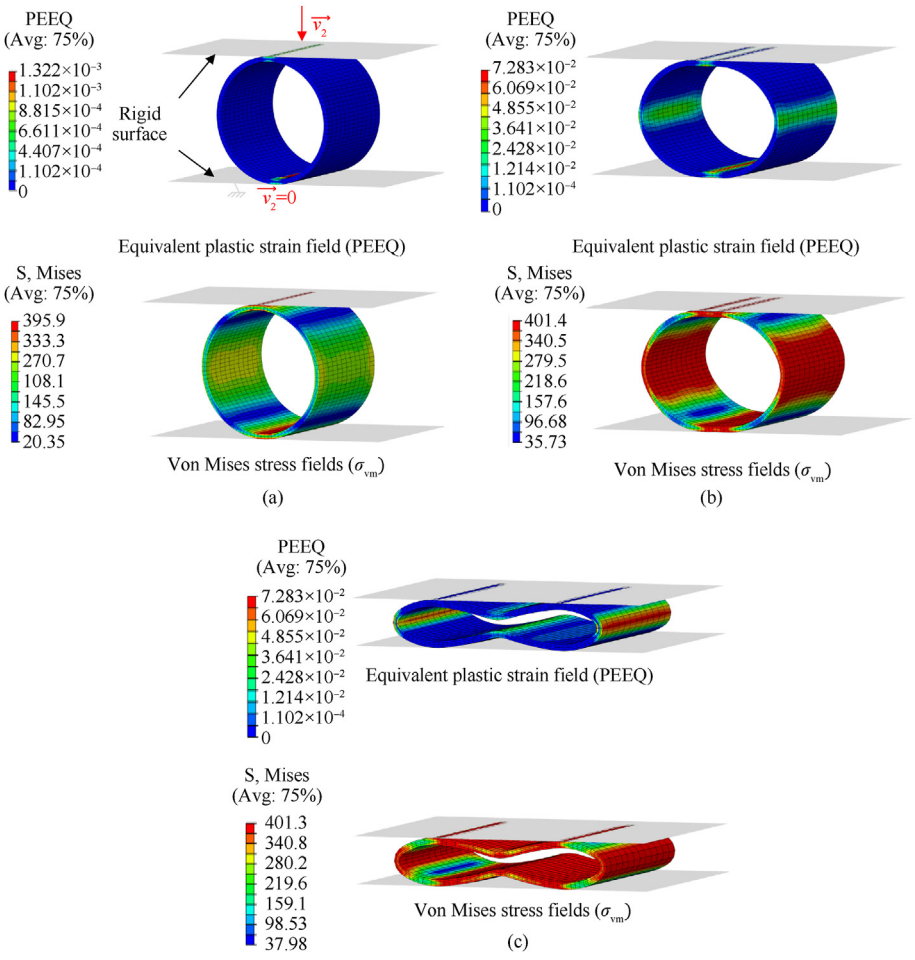

Fig. 14. Von Mises stress (in MPa) and plastic strain (PEEQ) fields during the simulation carried out at 3 mm/min and 293 K: (a) $t = 4$ s/$d = 0.2$ mm; (b) $t = 33$ s/$d = 1.65$ mm; (c) $t = 130$ s/$d = 6.5$ mm.

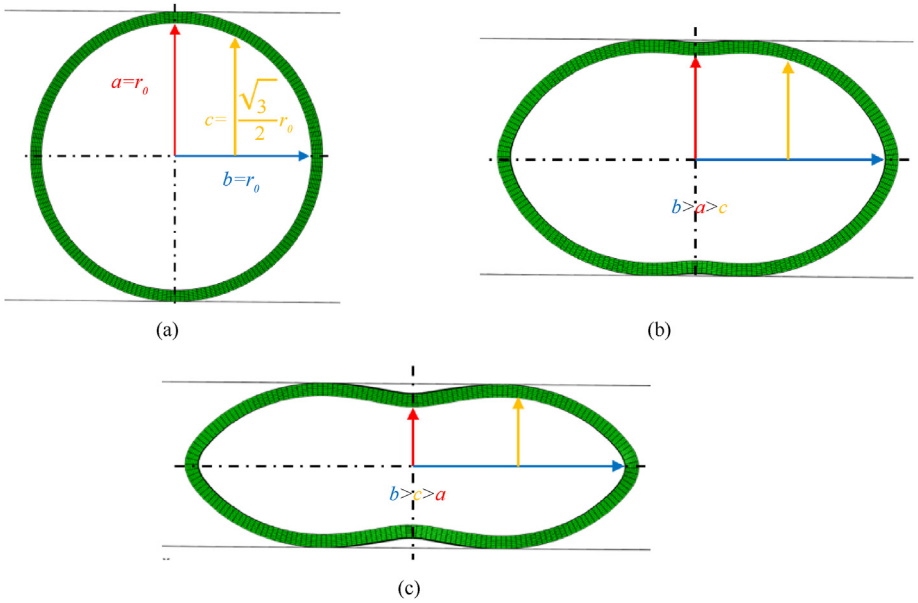

Fig. 15. Geometrical parameters characterizing the shape of the sample cross section: (a) Initial configuration with $b = a = r_0$, the initial internal radius of the ring, and $c = \sqrt{3}/2r_0$; (b) Oval shape with $b > a > c$; (c) Bow tie shaped where $b > c > a$.

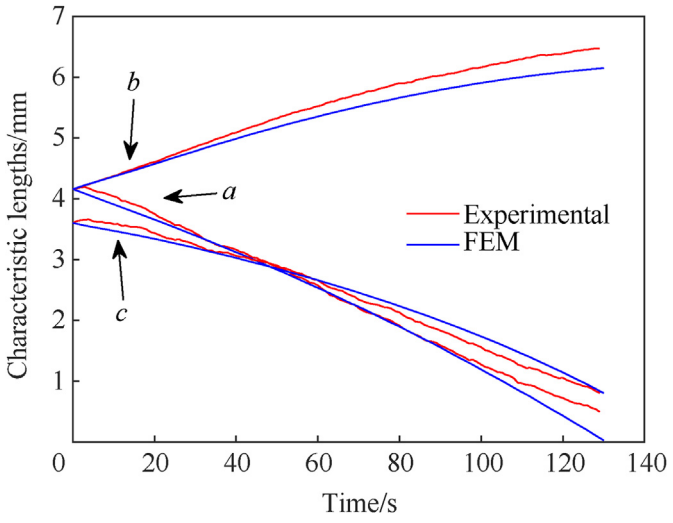

Fig. 16. Time evolution of characteristic lengths *a*, *b*, *c* for the compression test conducted at a traverse speed of 3 mm/min and room temperature (293 K). Comparison between experimental and FEM results.

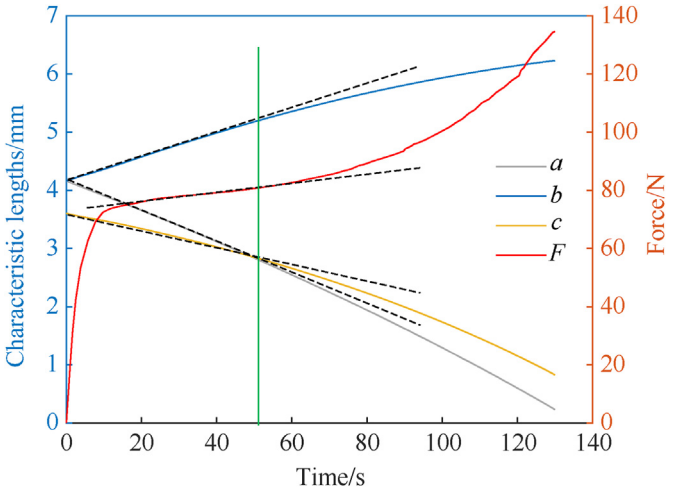

Fig. 17. Time evolution of characteristic lengths *a*, *b*, *c* (left axis) and force (right axis) for the test conducted at 3 mm/min under room temperature ($T = T_0 = 293$ K), and corresponding linear fits in dashed lines.

extracted from the ammunition, to validate the constitutive modeling of the entire ammunition system. The comparison between the numerical and experimental strain measurements at both input and output bar gauges revealed a compelling correlation, reaffirming the accuracy of our numerical predictions based on the identified parameters.

For analysis purposes, the current shape of the sample's cross section is characterized by three specific length parameters, see Fig. 15. Parameters *a* and *b* stand for the vertical and horizontal, mid distances between cylinder's walls, respectively. The length *c* corresponds to the vertical mid distance determined at the middle of b. Initially, $b = a = r_0$, the initial internal radius of the thin cylinder, while $c = \frac{\sqrt{3}}{2} r_0 < a$. Under applied loading, the dominant deformation mode of the cross section evolves from a circular ($b = a > c$, Fig. 15(a)) to an oval shape ($b > a > c$, Fig. 15(b)) then adopts a bow tie shape ($b > c > a$, Fig. 15(c)).

Fig. 16 proposes a comparison between experimental and numerical results showing the time evolution of the characteristic lengths *a*, *b* and *c*, defined in Fig. 15. Despite some differences, the agreement between simulations and experimental is still acceptable and allow to validate the model used to couple the method of optimization.

The numerical results are now isolated in order to highlight relationships between length parameters and the force-displacement curve. Fig. 17 presents the time evolution of lengths *a*, *b* and *c* (left axis) as well as the force (right axis) for the test conducted at 3 mm/min at 293 K. One observes that *a* and *b* evolve in a linear manner up to a critical time $t = t^* \approx 50$ s which falls close to the end of Stage III (as defined in subsection 4.1.1, Fig. 6). Interestingly, from Fig. 17, it appears that $t \times$ is well characterizing the point where *a* and *c* intercepts, thus identifying the time at which the cross-section changes from an oval to a bow tie shape. At the end of the test, *a* is close to zero meaning that the top and bottom parts of the ring are nearly in contact inducing a compaction process.

Using numerical simulation, a parametric study is reported.

5. Parametric study of friction coefficient and hardening parameters

This section aims to study the friction coefficient effect and the hardening parameters B and n on the numerical estimations to explain experimental tests. The numerical modeling described in subsection 3.3 is used with prescribed velocity of 3 mm/min and temperature of 293 K. The reference set of parameters reported in Table 3 is adopted, except otherwise specified.

5.1. Influence of the friction coefficient on the force and deformation during lateral compression test

This section focuses on the influence of the friction coefficient *f*, between the sample and the compression platens. Fig. 18 displays numerical force-displacement curves obtained when *f* is varying from 0.05 to 1. One observes that the two first stages (as defined in Fig. 6) are not depending on *f* while Stages III and IV are only slightly influenced by the friction coefficient. Between the lowest friction coefficient of 0.05 and the highest value of 1, there is a slight increase of about 7 % in the force at a displacement of 6.5 mm.

Fig. 19 portrays the final shape of the front section of the specimen obtained at $t = 130$ s (i.e. at a displacement of 6.5 mm) for

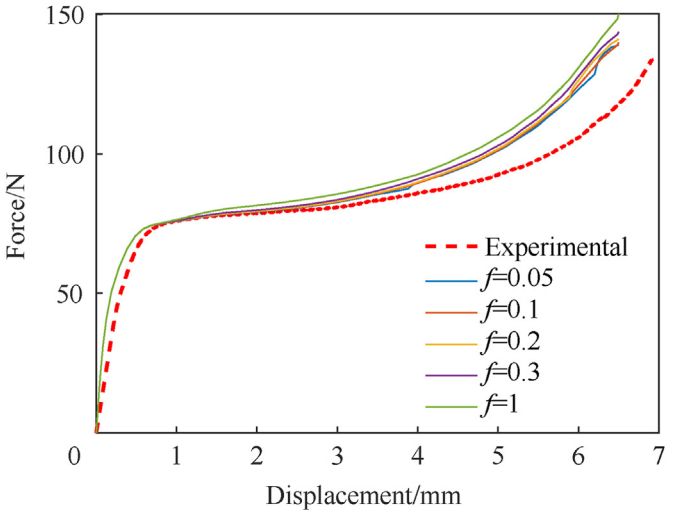

Fig. 18. Influence of the friction coefficient f on force-displacement curves for the test at 3 mm/min and 293 K.

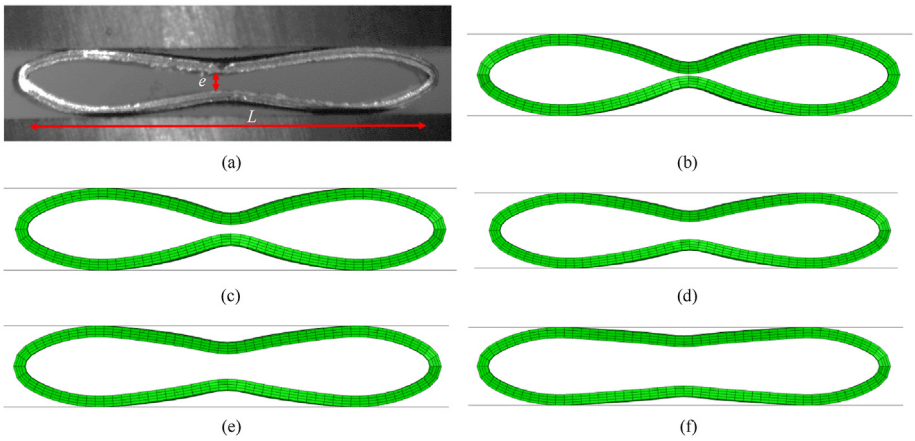

Fig. 19. Comparison of the front cross section at $t = 130$ s (i.e. a displacement of 6.5 mm) for different values of the friction coefficient for the test at 3 mm/min for 293 K: (a) Experimental; (b) $f = 0.05$; (c) $f = 0.1$; (d) $f = 0.2$; (e) $f = 0.3$; (f) $f = 1$.

various values of the friction coefficient f. In contrast with the negligible influence of f on the force-displacement curves, the effect of friction is more remarkable on the ring cross section. For a very low value of $f = 0.05$, the sample has a pronounced bow tie shape while when $f = 1$, the ring exhibits a more oval shape. The comparison with the experimental case (Fig. 19(a)) points out that the value of $f = 0.2$ (Fig. 19(d)) gives a better rendering of the experimental shape.

It finally appears that the value of f has a negligible influence on the force-displacement curve such that an adjustment of this parameter could not provide a better restitution of the experimental data (see Fig. 18). However, the friction coefficient strongly influences the deformation of the sample. The value of 0.2, which was found as an optimal value able to reproduce the experimental shape, has been adopted in the present paper.

5.2. Influence of the hardening parameters B and n

As previously mentioned, the values of B and n identified in subsection 4.2.2 are low compared to the set of values reported in the literature for mild steels, see Table 3. This may be explained by the hardening and possible thermal treatment undergone by the material while forming the jacket but can also find explanation in the practical identifiability of the hardening parameters from the ring diametral compression test. The aim here is not to apply the parameters' identifiability framework [44,45], but to develop a better understanding of the interplay between B and n. This is done by examining, from a numerical point of view, the effect of the hardening parameters on the force-displacement curve and the deformation of the front cross section. The test at 3 mm/min and 293 K is considered in this section.

Let first concentrate on the influence of the hardening exponent by varying n between 0.1 and 0.96 for a constant value of B. The maximal tested value of $B = 400$ MPa is chosen so as to better highlight a potential effect of n. Fig. 20 emphasizes that n has an effect on two characteristics of the force-displacement curve. First, an increase in n leads to an increase in the force at the end of stage II. Second, as n is enhanced, the slope of the force-displacement curve, dF/dd, is reduced in stage III, while it is slightly affected in the last stage IV. A large value of n thus provides a better restitution of the limited growth of the force observed in experiment during stage III.

The influence of B is now examined in the range from 0 MPa to 400 MPa for the fixed reference value of $n = 0.96$, which inferred the most limited increase of the force during stage III. Fig. 21 presents the influence of the parameter B on the force-displacement

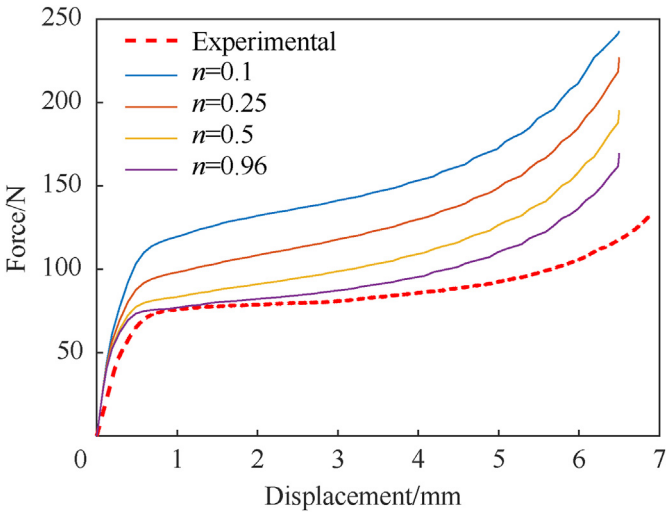

Fig. 20. Force-displacement curves obtained for the test at 3 mm/min and 293 K. Influence of the strain hardening parameter n for $B = 400$ MPa.

curve for the test conducted at 3 mm/min and $T = 293$ K. It appears that the value of B has very little influence on Stage II while it naturally does not affect Stage I. An increase of B induces a small increase of the slope dF/dd in Stage III which in turns induces a larger force. At the end of Stage IV, the maximal deviation between the tested configurations is about 13.5%.

A complementary case has been evaluated. Fig. 21(b) shows the force-displacement curves considering the reference value of $B = 1$ MPa and two values of n: 0.96 corresponding to the reference value and 0.1. Due to the very low value of B, the two curves are superimposed.

5.3. Influence of constitutive model parameters B and n on the ring shape on the deformation kinematics during lateral compression test

The test at 3 mm/min at room temperature ($T = 293$ K) is considered adopting three sets of hardening parameters (all other parameters being taken from Table 3): $B = 1$ MPa, $n = 0.96$, corresponding to the identified set of hardening parameters, and two simulations which showed the highest sensitivity on the force-displacement curves of Fig. 22 ($B = 400$ MPa/$n = 0.96$ and

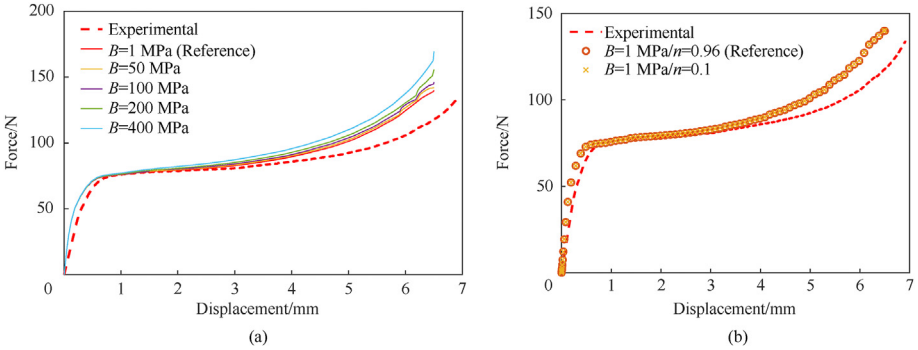

Fig. 21. Force-displacement curves obtained for the test at 3 mm/min and 293 K: (a) Influence of the parameter B for $n = 0.96$; (b) influence of the strain hardening exponent n when $B = 1$ MPa.

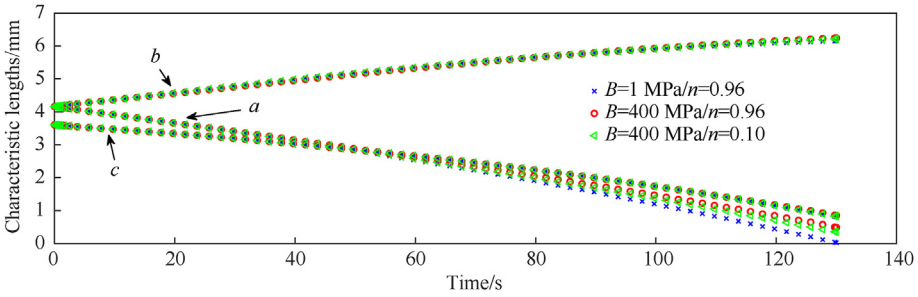

Fig. 22. Time evolution of lengths *a*, *b* and *c* characterizing the cross section obtained from numerical simulations (traverse speed of 3 mm/min, temperature of 293 K). Three values of (B, n) have been considered: (1 MPa, 0.96), corresponding to the identified set of hardening parameters, (400 MPa, 0.96), (400 MPa, 0.1). All other parameters are listed in Table 3.

$B = 400$ MPa/$n = 0.1$).

Results are reported in Fig. 22, showing the time evolution of the characteristic lengths *a*, *b* and *c*. Clearly, the results are very similar whatever the studied case, meaning that the shape evolution is only little influenced by the tested sets of hardening parameters. Recall that the experimental result revealed a faster evolution of *b* (see Fig. 16). From our results, it seems that the reduction of this difference would not benefit from an adjustment of hardening parameters.

To conclude, this analysis emphasizes the interplay between *B* and *n*. A small value of *B* mitigates the effect of *n* and a value of *n* close to 1 (i.e. linear hardening) plays a similar role with respect to *B*. It has also to be pointed out that the macroscopic behavior obtained from lateral compression tests on thin cylinders may include a non-negligible part of structural response which makes difficult to be so discriminant on the hardening parameters. In other words, the identified parameters are intended solely for characterizing the mechanical properties of the steel grade within the confines of the ring geometry and the unique forming process employed in shaping the thin ammunition jacket. Notably, the large value of *n* and the low value of *B* – an unusual observation within the existing literature on this type of steel – both contribute to better reflect the slight force increment observed during Stage III.

6. Conclusions

In this paper, the mechanical properties of a 9 mm small caliber steel jacket were studied to determine the parameters of the constitutive Johnson-Cook model. Experimental lateral compression tests on ring-shaped specimens directly extracted from the bullets were conducted under various strain rates and temperature conditions. Due to the particularly small and thin dimensions of the rings, these tests did not allow us to obtain classical stress-strain curves. Thereby, an inverse optimization method using LS-OPT© and Abaqus/Standard was implemented to identify the parameters of the constitutive model from the measured force-displacement curves. It is worth highlighting that the numerical model inherently addresses the complex loading state that arises during the deformation of the ring specimen, which includes both shear and bending stresses.

The optimization procedure utilized three objective functions, one corresponding to the force-displacement curve obtained for a specific loading condition (speed of 3 mm/min and room temperature), while the other two were constructed from specific data points collected from all force-displacement curves. By implementing this testing and optimization method, we preserved the jacket material properties and geometry in their original state, contributing to the accuracy of the constitutive model.

Furthermore, numerical simulations conducted with the FEM software Abaqus/Standard were employed to validate the model by comparing the experimental and numerical force-displacement curves, as well as the deformation of the cross-sections. While our numerical results did not capture the late stage of the deformation process, the simulations and discussions highlighted that the material could be effectively described by a model that incorporates strain rate and temperature sensitivities, without the need for strain hardening dependencies. The limited sensitivity to hardening, an uncommon observation for this type of steel in the literature, can be attributed to the specific ring geometry (thus reflecting partly a structural response), forming process used in shaping the thin ammunition's jacket and its inherent deformation history.

Apart from its validation purpose, the numerical model was employed to investigate the connection between the characteristics of the force/displacement curve and the configuration of the cross-section. Besides, an examination of the friction sensitivity between

tools and the sample revealed that this parameter primarily influences the deformation shape of the sample and not the measured forces.

A comprehensive numerical model-based analysis of the interplay between parameters *B* and *n* of the Johnson-Cook law revealed that the shape of the cross section is little influenced while these parameters have a marked effect on force-displacement curves. Notably, the main differences between numerical and experimental results were observed during the final stage of the test when the sample underwent large deformations. A closer examination of the post-mortem sample showed the occurrence of a folding-type instability in regions of the ring where plastic deformation localized. Our study focused mainly on the elastic and plastic behavior of the structural part, prior the occurrence of any instability. Moreover, while this observation may explain the deviations observed in the force-displacement curves between numerical and experimental values at late stages, it is important to note that this type of deformation mode is not typically encountered in ballistic impacts.

Additionally, during all of the ring diametral compression tests, the traverse speed was limited to 3 mm/min, constraining the study to the low strain rate regime. Due to the geometry of the sample, it was not possible to conduct dynamic experiments (e.g., using the Split Hopkinson apparatus) on the jacket extracted from the ammunition. Nonetheless, it is noteworthy that the identified value of the C parameter of the Johnson-Cook model, which captures the strain rate effect, is in the same order of magnitude as values reported in the literature for mild steels and identified using high strain rate experiments. It is important to highlight that the set of parameters obtained in this paper has been effectively used to describe the dynamic response of a cylinder comprising a lead core and the steel jacket used here with sufficient accuracy [2]. This validation highlights the practical applicability of our findings.

In summary, the results presented in this work should be viewed as a preliminary investigation, which requires further complementation through dynamic characterization and validation, i.e. considering the full bullet system under ballistic impact. Ultimately, these efforts will enable us to numerically describe the ballistic performance of protective equipment when subjected to the impact of such ammunition, further demonstrating the applicability of the identified parameters.

Funding

This study is co-funded by the Direction Générale de l'Armement (DGA) and the French-German Institute of Saint Louis (ISL).

Declaration of competing interest

The authors declare that they have no known competing financial interests or personal relationships that could have appeared to influence the work reported in this paper.

Acknowledgments

The authors would like to thank ISL services collaborating in the design and implementation of the tests and analyses.

References

[1] Coget Y, Demarty Y, Rusinek A. Characterization of the mechanical behavior of a lead alloy, from quasi-static to dynamic loading for a wide range of temperatures. Materials 2020;13(10):2357. https://www.mdpi.com/1996-1944/13/10/2357.

[2] Coget Y, Novak J, Gütter G, Demarty Y, Rusinek A. Dynamic testing and simulation of 9 mm full metal jacket ammunition. EPJ Web Conf 2021;250:05002. https://doi.org/10.1051/epjconf/202125005002.

[3] Adams B. Simulation of ballistic impacts on armored civil vehicles. Master Thesis. Technische Universiteit Eindhoven; 2006. p. 101. https://research.tue.nl/en/studentTheses/simulation-of-ballistic-impacts-on-armored-civil-vehicles.

[4] Peroni L, Scapin M, Fichera C, Manes A, Giglio M. Mechanical properties at high strain-rate of lead core and brass jacket of a NATO 7.62 mm ball bullet. EPJ Web Conf 2012;(26):01060. https://doi.org/10.1051/epjconf/20122601060.

[5] Marechal C, Bresson F, Haugou G. Development of a numerical model of the 9 mm Parabellum FMJ bullet including jacket failure. Eng Trans 2011;59(4):263–72.

[6] Gilson L, Rabet L, Imad A, Coghe F. Experimental and numerical assessment of non-penetrating impacts on a composite protection and ballistic gelatine. Int J Impact Eng 2020;136:103417. https://doi.org/10.1016/j.ijimpeng.2019.103417.

[7] Simon P, Demarty Y, Rusinek A, Voyiadjis GZ. Material behavior description for a large range of strain rates from low to high temperatures: application to high strength steel. Metals 2018;10(8):795. https://doi.org/10.3390/met8100795.

[8] Markiewicz E, Ducrocq P, Drazetic P. An inverse approach to determine the constitutive model parameters from axial crushing of thin-walled square tubes. Int J Impact Eng 1998;(21):433–49. https://doi.org/10.1016/S0734-743X(98)00004-9.

[9] Baroutaji A, Morris E, Olabi AG. Quasi-static response and multi-objective crashworthiness optimization of oblong tube under lateral loading. Thin-Walled Struct 2014;82:262–77. https://doi.org/10.1016/j.tws.2014.03.012.

[10] Rojíček J, Čermák M, Halama R, Paška Z, Vaško M. Material model identification from set of experiments and validation by DIC. Math Comput Simulat 2021;(189):339–67. https://doi.org/10.1016/j.matcom.2021.04.007.

[11] Martins JMP, Thuillier S, Andrade-Campos A. Calibration of a modified Johnson-Cook model using the Virtual Fields Method and a heterogeneous thermo-mechanical tensile test. Int J Mech Sci 2021;202–203:106511. https://doi.org/10.1016/j.ijmecsci.2021.106511.

[12] Mathieu N, Czarnota C, Obeid H, Mercier S. Prediction of flatness defects and of the stable configuration of thin multilayer assemblies due to chemical shrinkage. Computational Materials Science 2022;210:111389. https://doi.org/10.1016/j.commatsci.2022.111389.

[13] Markiewicz E, Langrand B, Notta-Cuvier D. A review of characterisation and parameters identification of materials constitutive and damage models: from normalised direct approach to most advanced inverse problem resolution. Int J Impact Eng 2017;110:371–81. https://doi.org/10.1016/j.ijimpeng.2017.01.028.

[14] Bracq A, Brest J-S, Abrantes de Sampaio J, Moitrier F, Demarty Y. Characterization and modelling of the mechanical behaviour of metal rings: application to a brass bullet jacket. Forces in Mechanics 2021;4:100030. https://doi.org/10.1016/j.finmec.2021.100030.

[15] Al-Shemmary A, Hashim F, Salim S. Collapse behavior of thin-walled cylinder tubes under quasi-static axial loading. AIP Conf Proc 2020;2307:020011. https://doi.org/10.1063/5.0032992.

[16] Lin Y, Min J, Li Y, Lin J. A thin-walled structure with tailored properties for axial crushing. Int J Mech Sci 2019;157(-158):119–35. https://doi.org/10.1016/j.ijmecsci.2019.04.015.

[17] Gupta NK, Sekhon GS, Gupta PK. Study of lateral compression of round metallic tubes. Thin-Walled Struct 2005;43(6):895–922. https://doi.org/10.1016/j.tws.2004.12.002.

[18] Sinaie S, Ngo TD, Nguyen VP, Rabczuk T. Validation of the material point method for the simulation of thin-walled tubes under lateral compression. Thin-Walled Struct 2018;130:32–46. https://doi.org/10.1016/j.tws.2018.05.014.

[19] Shabani B, Rad SG, Alijani A, Darvizeh A, Rajabiehfard R. Dynamic plastic behavior of single and nested rings under lateral impact. Thin-Walled Struct 2021;160:107373. https://doi.org/10.1016/j.tws.2020.107373.

[20] Garrison B, Yan Y, TerMaath S. Determining failure properties of as-received and hydrided unirradiated Zircaloy-4 from ring compression tests. Eng Fail Anal 2021;(125):105362. https://doi.org/10.1016/j.engfailanal.2021.105362.

[21] Nemat-Alla M. Reproducing hoop stress–strain behavior for tubular material using lateral compression test. Int J Mech Sci 2003;45(4):605–21.

[22] Bizet L, Charleux L, Balland P, Tabourot L. Influence of heterogeneities introduced into the modelling of a ring compression test. Arch Civ Mech Eng 2017;17(2):365–74. https://doi.org/10.1016/j.acme.2016.11.002.

[23] Rathnaweera G, Durandet Y, Ruan D, Kinoshita S. Characterizing the material properties of a tube from a lateral compression test. Int J Prot Struct 2011;2(4):465–75. https://doi.org/10.1260/2041-4196.2.4.465.

[24] Chen H, Cai LX. Unified ring-compression model for determining tensile properties of tubular materials. Mater Today Commun 2017;(13):210–20. https://doi.org/10.1016/j.mtcomm.2017.10.006.

[25] Han GZ, Bao C, Liang B, Lv Y, Huang MB, Liu XK. Novel ring compression test method to determine the stress-strain relations and mechanical properties of metallic materials. Chin J Mech Eng 2021;34:109. https://doi.org/10.1186/s10033-021-00622-y.

[26] Pavlina EJ, Van Tyne CJ. Correlation of yield strength and tensile strength with hardness for steels. J Mater Eng Perform 2008;(17):888–93. https://doi.org/10.1007/s11665-008-9225-5.

[27] Fujita M, Kuki K. An evaluation of mechanical properties with the hardness of building steel structural members for reuse by NDT. Metals 2016;(6):247.

https://doi.org/10.3390/met6100247.
[28] Iqbal MA, Senthil K, Sharma P, Gupta NK. An investigation of the constitutive behavior of Armox 500T steel and armor piercing incendiary projectile material. Int J Impact Eng 2016;(96):146–64. https://doi.org/10.1016/j.ijimpeng.2016.05.017.
[29] Xu Z, Huang F. Plastic behavior and constitutive modeling of armor steel over wide temperature and strain rate ranges. Acta Mech Solida Sin 2012;25(6):598–608. https://doi.org/10.1016/S0894-9166(12)60055-X.
[30] Bobbili R, Madhu V. Constitutive modeling of hot deformation behavior of high-strength armor steel. J Mater Eng Perform 2016;25(5):1829–38. https://doi.org/10.1007/s11665-016-2001-z.
[31] Zerilli FJ, Armstrong RW. Dislocation-mechanics-based constitutive relations for material dynamics calculations. J Appl Phys 1987;61(5):1816. https://doi.org/10.1063/1.338024.
[32] Rusinek A, Klepaczko JR. Shear testing of a sheet steel at wide range of strain rates and a constitutive relation with strain-rate and temperature dependence of the flow stress. Int J Plast 2001;(17):87–115. https://doi.org/10.1016/S0749-6419(00)00020-6.
[33] Preston DL, Tonks DL, Wallace DC. Model of plastic deformation for extreme loading conditions. J Appl Phys 2003;(93):211–20. https://doi.org/10.1063/1.1524706.
[34] Johnson K. Contact mechanics. Cambridge: Cambridge University Press; 1985. https://doi:10.1017/CBO9781139171731.
[35] Cooreman S. Identification of the plastic material behavior through full-field displacement measurements and inverse methods. Doctoral thesis. Belgium: Free University of Brussels; 2008.
[36] Kleijnen JPC. Kriging metamodeling in simulation: a review. Eur J Oper Res 2009;192(3):707–16. https://doi.org/10.1016/j.ejor.2007.10.013.
[37] Stander N, Basudhar A, Roux W, Witowski L, Eggleston T, Goel T, Craig K. LS-OPT® user's manual, version 6.0. Livermore Software Technology Corporation; 2019.
[38] Pascu A, Oleksik V, Bondrea I, Roşca L. Inverse analysis used to determine plastic flow and tribological characteristics for deep-drawing sheet. Procedia Eng 2014;81:1823–9. https://doi.org/10.1016/j.proeng.2014.10.240.
[39] Gavrus A, Massoni E, Chenot JL. The rheological parameter identification formulated as an inverse finite element problem. Inverse Probl Eng 1999;7(1):1–41. https://doi.org/10.1080/174159799088027685.
[40] section 2.3.5 Abaqus online documentation version 6.6-1. ABAQUS, Inc; 2006.
[41] Gilson L. Etude du comportement mécanique des multi-matériaux soumis à un impact balistique : approches expérimentale et numérique. Doctoral thesis, Université de Lille 2017;1:223. http://www.theses.fr/2017LIL10190.
[42] Wiśniewski A, Pacek D. Experimental research and numerical analysis of 9 mm Parabellum projectile penetration of ultra-high molecular weight polyethylene layers. Problemy Techniki Uzbrojenia 2013;42(127):55–64. https://bibliotekanauki.pl/articles/235372.
[43] Reddy TY, Reid SR. On obtaining material properties from the ring compression test. Nucl Eng Des 1979;52(2):257–63.
[44] Brun R, Reichert P, Künsch HR. Practical identifiability analysis of large environmental simulation models. Water Resour Res 2001;37(4):1015–30. https://doi.org/10.1029/2000WR900350.
[45] Zhang Y, Van Bael A, Andrade-Campos A, Coppieters S. Parameter identifiability analysis: mitigating the non-uniqueness issue in the inverse identification of an anisotropic yield function. Int J Solid Struct 2022;243:111543. https://doi.org/10.1016/j.ijsolstr.2022.111543.